Generation of pulse trains with nonconventional temporal correlation properties

Ria Talukder[1,2], Atri Halder[1], Matias Koivurova[3,4], Chaoliang Ding[5], Tero Setälä[1], Jari Turunen[1] and Ari T. Friberg[1]

[1]Institute of Photonics, University of Eastern Finland, 80100 Joensuu, Finland
[2]Institut FEMTO-ST, UMR6174, CNRS Université Bourgogne Franche-Comté, 15B Avenue des Montboucons, 25030 Besançon cedex, France
[3]Tampere Institute for Advanced Study, Tampere University, 33100 Tampere, Finland
[4]Faculty of Engineering and Natural Sciences, Tampere University, 33720 Tampere, Finland
[5]Department of Physics and Henan Key Laboratory of Electromagnetic Transformation and Detection, Luoyang Normal University, Luoyang 471934, China

E-mail: atri.halder@uef.fi

March 2022

Abstract. We apply time dependent spectral phase modulation to generate pulse trains that are spectrally and temporally partially coherent in an ensemble averaged sense. We consider, in particular, quadratic spectral phase modulation of Gaussian pulses, and demonstrate two particular types of nonuniformly correlated pulse trains. The controlled partial temporal coherence of the nonstationary fields is generated using a pulse compressor and experimentally verified with frequency resolved optical gating (FROG). We show that the correlation characteristics of such pulse trains can be retrieved directly from the FROG spectrograms provided one has certain *a priori* knowledge of the pulse train. Our results open a pathway for experimental confirmation of several correlation induced effects in the temporal domain.

1. Introduction

Partial coherence has been extensively studied over the past several decades, with emphasis on modeling, generating, and characterizing spatially partially coherent fields [1, 2]. Recent studies have revealed that statistically stationary, partially coherent beam-like fields exhibit unexpected propagation properties, such as self-focusing [3–5], self-splitting [6, 7], self-steering [8], and enable various types of beam profile transformations [9–16]. The emphasis on spatial domain has been motivated by the experimentally available methods for generating spatially partially coherent fields.

In addition to spatially partially coherent fields, a large number of temporally partially coherent model pulse trains have been theoretically introduced [17–20], with several potential applications including temporal ghost imaging [21–23], inertial confinement fusion [24–26], telecommunication [27–29], and micro-machining [30, 31], to name a few. Many of these statistically nonstationary fields have time-domain coherence properties that are quite analogous to the spatial coherence of the stationary beam fields. However, at present, there is a severe lack of flexible and reliable methods to produce temporally partially coherent pulse trains with tailored coherence properties. In the present study, we experimentally demonstrate such a method and apply it to generation of pulse trains with nonconventional temporal correlation functions.

We consider the individual pulses in a pulse train as field realizations, in which case the second-order statistical properties of the train can be described by ensemble averaged two-coordinate correlation functions, namely the two-frequency cross-spectral density function (CSD) and the two-time mutual coherence function (MCF) [32–34]. When employing this notion for coherence, the pulse train is fully coherent only if the pulses have identical wave forms and are equidistant within the train; otherwise the train becomes partially coherent.

The two-frequency CSD and the two-time MCF admit specific formal representations, summarized in Sec. 2, which ensure that the CSD and MCF necessarily are genuine coherence functions and, furthermore, provide a recipe for constructing pulse trains with specified coherence properties. A large class of model pulse trains can be realized by modulating the spectral phases of the pulses of a coherent train. The simplest way to do this is to introduce a quasi-random linear phase, which leads to a jittered output train of pulses with the same temporal shape, formally allowing the realization of a variety of conventional Schell-model correlated pulse trains [35]. However, jitter alone constitutes a limited means to control pulse train coherence and, moreover, it is not observable with most pulse characterization methods, due to arrival time ambiguities. Therefore, here we examine quadratic spectral phase modulation, and as explicit demonstrations introduce pulse trains with two specific types of nonconventional temporal correlation functions.

The spectral and temporal wave forms of individual pulses can readily be obtained, for instance, by frequency resolved optical gating (FROG) [36]. However, partial coherence smears multishot FROG spectrograms, rendering direct retrieval of the coherence properties (or even average pulse shapes) ambiguous in most cases [37]. We show in Sec. 3 that the relevant characteristic parameters of the pulse trains we consider can nonetheless be directly deduced from FROG spectrograms, without any need for retrieval, provided that the generic type of the pulse train is known *a priori*.

Furthermore, in Sec. 4, we prove the practical feasibility of our proposed temporal coherence tailoring scheme by presenting experimental results, based on modulating the spectral phases of mode-locked femtosecond laser pulses with the aid of a phase-only spatial light modulator (SLM) [38] and characterizing the ensuing output pulses by FROG. Specifically, we generate the temporal versions of circularly correlated [39, 40] and certain spatially nonuniformly correlated light beams [3, 41, 42]. The protocol of controlling statistical temporal coherence of pulse trains, combined with experimental SLM-based creation of two specific nonconventional temporal coherence functions, and the explicit demonstration of retrieving, under certain prior knowledge, the salient coherence features of the modulated pulse train directly from FROG spectrograms constitute the main results of this work.

Finally, in Sec. 5, we present concluding remarks and outline some possible future directions.

2. Theory

Let us denote the spectral representation of an individual plane-wave pulse in the train by $E_n(\omega)$.

Then the two-frequency CSD is, by definition, given by

$$W(\omega_1,\omega_2) = \langle E^*(\omega_1)E(\omega_2)\rangle = \lim_{N\to\infty}\frac{1}{N}\sum_{n=1}^{N} E_n^*(\omega_1)E_n(\omega_2). \quad (1)$$

Its normalized form, known as the two-frequency complex degree of spectral coherence, is defined as

$$\mu(\omega_1,\omega_2) = \frac{W(\omega_1,\omega_2)}{\sqrt{S(\omega_1)S(\omega_2)}}, \quad (2)$$

where $S(\omega) = W(\omega,\omega)$ is the (mean) spectral density of the pulse train.

The time-domain representations of the individual pulse realizations are related to the frequency-domain realizations by a Fourier transform

$$E_n(t) = \int_0^\infty E_n(\omega)\exp(-i\omega t)\mathrm{d}\omega. \quad (3)$$

In analogy with Eq. (1), one defines the two-time MCF as

$$\Gamma(t_1,t_2) = \langle E^*(t_1)E(t_2)\rangle = \lim_{N\to\infty}\frac{1}{N}\sum_{n=1}^{N} E_n^*(t_1)E_n(t_2). \quad (4)$$

Its normalized form, known as the two-time complex degree of temporal coherence, is

$$\gamma(t_1,t_2) = \frac{\Gamma(t_1,t_2)}{\sqrt{I(t_1)I(t_2)}}, \quad (5)$$

where $I(t) = \Gamma(t,t)$ is the (mean) temporal intensity of the pulse train.

Let us now assume that the spectral realizations can be expressed as a continuous function of a parameter c, i.e., $E(\omega;c)$. Then the CSD has a (genuine) representation [43]

$$W(\omega_1,\omega_2) = \int_{-\infty}^{\infty} p(c)E^*(\omega_1;c)E(\omega_2;c)\mathrm{d}c, \quad (6)$$

where $p(c)$ is a real and non-negative weight function and $\int_{-\infty}^{\infty} p(c)\mathrm{d}c = 1$. Correspondingly, the MCF is given by

$$\Gamma(t_1,t_2) = \int_{-\infty}^{\infty} p(c)E^*(t_1;c)E(t_2;c)\mathrm{d}c, \quad (7)$$

where the temporal realizations $E(t;c)$ are obtained by a Fourier relationship analogous to Eq. (3).

In what follows, we assume that the spectral envelope of each pulse has the same functional form but the spectral phase may vary from pulse to pulse. Then we may write

$$E(\omega;c) = A_0(\omega-\omega_0)\exp[i\phi(\omega;c)], \quad (8)$$

where the envelope, $A_0(\omega-\omega_0)$, may in general be complex and ω_0 is the central frequency of the mean spectrum. Here we consider quadratic phase modulation with

$$\phi(\omega;c) = c(\omega-\omega_0)^2. \quad (9)$$

While the role of the parameter c is generally rather formal, its physical significance becomes clear as soon as we specify the form of the weight function $p(c)$ and the spectral phase of the pulses. With the quadratic spectral phase in Eq. (9), c represents the phase curvature at the center frequency. Increasing $|c|$ also increases the curvature of the spectral phase, whereas $c = 0$ corresponds to flat spectral phase, i.e., a transform-limited pulse. Non-zero values of c mean concave or convex parabolic phase, which both lead to wider pulses in the time domain. This quadratic phase is considered throughout the paper.

With the choice of a parabolic phase according to Eq. (9), the CSD can be written as

$$W(\omega_1,\omega_2) = A_0^*(\omega_1-\omega_0)A_0(\omega_2-\omega_0)\mu(\omega_1,\omega_2), \quad (10)$$

where

$$\mu(\omega_1,\omega_2) = \int_{-\infty}^{\infty} p(c) \times \exp\left\{ic\left[(\omega_2-\omega_0)^2-(\omega_1-\omega_0)^2\right]\right\}\mathrm{d}c. \quad (11)$$

In other words, the spectral correlation properties depend entirely on the weight function $p(c)$, and the envelope dictates only the shape of the spectrum. Corresponding to our experimental conditions, we choose a Gaussian spectral envelope

$$A_0(\omega-\omega_0) = A_0\exp\left[-\frac{(\omega-\omega_0)^2}{\Omega^2}\right], \quad (12)$$

where Ω represents the spectral width of the incident pulses. Pulse trains with nonconventional correlation functions can now be constructed by choosing different types of weight functions $p(c)$.

2.1. Circularly correlated pulse trains

Let us first choose a rectangular weight function

$$p(c) = \begin{cases} \Omega_\mathrm{p}^2, & \text{when } |c| \le 1/2\Omega_\mathrm{p}^2, \\ 0, & \text{otherwise,} \end{cases} \quad (13)$$

where Ω_p is the spectral coherence width. Then, from Eq. (11),

$$\mu(\omega_1,\omega_2) = \mathrm{sinc}\left[\frac{(\omega_2-\omega_0)^2-(\omega_1-\omega_0)^2}{2\Omega_\mathrm{p}^2}\right], \quad (14)$$

where $\mathrm{sinc}(x) = \sin(x)/x$. Equivalently, in average and difference coordinates $\bar{\omega} = \frac{1}{2}(\omega_1+\omega_2)$ and $\Delta\omega = \omega_2-\omega_1$, we have

$$\mu(\bar{\omega},\Delta\omega) = \mathrm{sinc}\left[\frac{(\bar{\omega}-\omega_0)\,\Delta\omega}{\Omega_\mathrm{p}^2}\right]. \quad (15)$$

The result is the spectral representation of a circularly correlated pulse train, which is a frequency-domain analog of the spatially circularly correlated field [39, 40].

To construct the MCF of a circularly correlated pulse train, we first transform the spectral field realizations into the time domain, which yields

$$E(t;c) = \exp(-i\omega_0 t) \times \int_{-\infty}^{\infty} A_0(\tilde{\omega}) \exp\left(ic\tilde{\omega}^2 - i\tilde{\omega}t\right) \mathrm{d}\tilde{\omega}. \quad (16)$$

Here we have denoted $\tilde{\omega} = \omega - \omega_0$ and extended the lower integration limit to $-\infty$, assuming that $\Omega \ll \omega_0$. Inserting from Eq. (12) and performing the integration we arrive at

$$E(t;c) = A_0 \frac{\sqrt{\pi}\Omega}{\sqrt{1 - i\Omega^2 c}} \exp\left(-\frac{\Omega^2}{4}\frac{t^2}{1 - i\Omega^2 c}\right) \times \exp\left(-i\omega_0 t\right). \quad (17)$$

The temporal intensity of a single field realization therefore has the form

$$I(t;c) = I_0(c) \exp\left[-\frac{2t^2}{T^2(c)}\right], \quad (18)$$

where $I_0(c) = 2\Gamma_0/\Omega T(c)$,

$$T(c) = T\sqrt{1 + \Omega^4 c^2}, \quad (19)$$

and $T = 2/\Omega$ is the temporal width of the incident transform-limited (unchirped) Gaussian pulses and $\Gamma_0 = \pi\Omega^2 |A_0|^2$.

In view of Eqs. (7) and (17), the MCF of a train of Gaussian pulses is given by

$$\Gamma(t_1, t_2) = \Gamma_0 \exp\left[-i\omega_0 (t_2 - t_1)\right] \int_{-\infty}^{\infty} \frac{p(c)}{\sqrt{1 + \Omega^4 c^2}} \times \exp\left[-\frac{\Omega^2}{4}\left(\frac{t_1^2}{1 + i\Omega^2 c} + \frac{t_2^2}{1 - i\Omega^2 c}\right)\right] \mathrm{d}c. \quad (20)$$

The integral can not be performed analytically, but it can be readily evaluated numerically.

2.2. Nonuniformly correlated pulse trains

As a second example we insert a Gaussian weight function

$$p(c) = \frac{1}{\sqrt{\pi}}\Omega_\mathrm{p}^2 \exp\left(-\Omega_\mathrm{p}^4 c^2\right), \quad (21)$$

in Eq. (11). We obtain

$$\mu(\omega_1, \omega_2) = \exp\left\{-\left[\frac{(\omega_2 - \omega_0)^2 - (\omega_1 - \omega_0)^2}{2\Omega_\mathrm{p}^2}\right]^2\right\}, \quad (22)$$

or, in average and difference coordinates,

$$\mu(\bar{\omega}, \Delta\omega) = \exp\left\{-\left[\frac{(\bar{\omega} - \omega_0)\,\Delta\omega}{\Omega_\mathrm{p}^2}\right]^2\right\}. \quad (23)$$

This is the complex degree of spectral coherence of a non-uniformly correlated pulse train [42]. The MCF of this pulse train is obtained on inserting from Eq. (21) into Eq. (20). Again the integral needs to be evaluated numerically.

2.3. General characteristics

Figure 1 illustrates the spectral coherence characteristics of the two types of pulse trains considered above. Here we plot the absolute values $|\mu(\tilde{\omega}_1, \tilde{\omega}_2)|$ of the complex degree of spectral coherence as functions of $\tilde{\omega}_1/\Omega_\mathrm{p}$ and $\tilde{\omega}_2/\Omega_\mathrm{p}$ in the case $\omega_0/\Omega_\mathrm{p} = 100$, which is close to our experimental conditions. The distributions of $|\mu(\tilde{\omega}_1, \tilde{\omega}_2)|$ feature a cross-like shape with diagonal and anti-diagonal arms. The nature of the correlations is therefore in both cases very different from those of Schell-model fields (where the complex degree of spectral coherence depends only on the coordinate difference $\Delta\omega$).

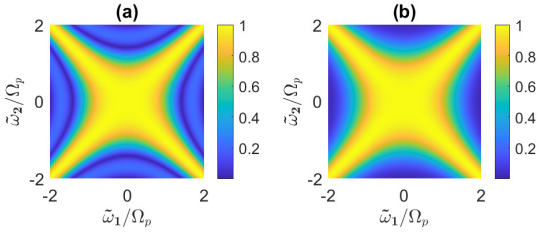

Figure 1. Absolute values of the complex degree of spectral coherence of (a) a circularly correlated, and (b) a nonuniformly correlated Gaussian pulse train.

The temporal coherence characteristics of the same pulse trains are illustrated in Fig. 2, where we plot the absolute values of the complex degree of temporal coherence as functions of t_1/T and t_2/T. Also the distributions of $|\gamma(t_1, t_2)|$ are cross-shaped [42].

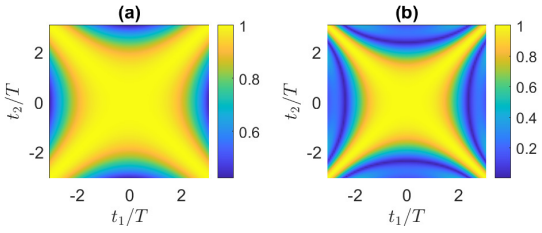

Figure 2. Absolute values of the complex degree of temporal coherence of (a) a circularly correlated, and (b) a nonuniformly correlated Gaussian pulse train.

The cross-like shape of the CSD is a result of it being of specular form, with the property $W(-\omega_1 + \omega_0, \omega_2 - \omega_0) = W(\omega_1 - \omega_0, \omega_2 - \omega_0)$. This property is the spectral analog of spatially partially coherent fields with specular CSDs, first introduced in [44] and more

recently demonstrated experimentally using wavefront-folding interferometry [45]. These specular light fields indeed represent an important class of optical fields that do not obey the often-used Schell model.

3. FROG spectrograms

In the experimental part of this work we will employ second-harmonic generation (SHG) FROG [36] to characterize the nonconventional pulse trains discussed above. This technique allows one to measure the amplitudes and phases of individual pulses (or coherent pulse trains) in both spectral and temporal domains. Once an ensemble of these realizations has been characterized, the CSD and the MCF of a partially coherent pulse train can be constructed using Eqs. (1) and (4), respectively.

Alternatively, to characterize unknown pulse trains, one can perform multishot SHG FROG measurements, i.e., measure spectrograms averaged over a large number of realizations. Unfortunately it is not possible to retrieve the CSD or the MCF of a partially coherent pulse train from these multishot spectrograms. However, as we will see below, the main characteristics of the pulse trains can be retrieved from such data provided that *a priori* knowledge on the type of the pulse train is available. We note that SHG FROG has two ambiguities: direction of time and arrival time. The latter implies that the effects of jitter are not visible in the spectrograms. However, the effect of quadratic phase modulation is observable.

The single-shot SHG FROG spectrogram of a temporal pulse $E(t;c)$ is given by

$$G(\omega,\tau;c) = |F(\omega,\tau;c)|^2, \tag{24}$$

where τ is the time delay and

$$F(\omega,\tau;c) = \int_{-\infty}^{\infty} E(t;c)E(t-\tau;c)\exp(i\omega t)\mathrm{d}t \tag{25}$$

is the (unmeasurable) complex spectrogram. If the incident pulses follow a weight distribution $p(c)$, the averaged spectrogram of the entire ensemble is

$$G(\omega,\tau) = \int_{-\infty}^{\infty} p(c)G(\omega,\tau;c)\mathrm{d}c. \tag{26}$$

On inserting from Eq. (17) into Eq. (25) we get

$$\begin{aligned} F(\omega,\tau;c) = {} & E_0^2(c)\exp\left(i\omega_0\tau\right) \\ & \times \int_{-\infty}^{\infty} \exp\left[-\frac{\Omega^2}{4}\frac{t^2+(t-\tau)^2}{1-i\Omega^2 c}\right] \\ & \times \exp\left[i\left(\omega-2\omega_0\right)t\right]\mathrm{d}t. \end{aligned} \tag{27}$$

Carrying out the integration and simplifying leads to

$$\begin{aligned} F(\omega,\tau;c) = {} & \pi\sqrt{2\pi}A_0^2\frac{\Omega}{\sqrt{1-i\Omega^2 c}}\exp\left(-\frac{\Omega^2}{8}\frac{\tau^2}{1-i\Omega^2 c}\right) \\ & \times \exp\left[-\left(1-i\Omega^2 c\right)\frac{\left(\omega-2\omega_0\right)^2}{2\Omega^2}\right]\exp(i\omega\tau/2). \end{aligned} \tag{28}$$

Hence, the spectrogram for a single pulse realization given by Eq. (24) is of the form

$$\begin{aligned} G(\omega,\tau;c) = {} & G_0\frac{T}{T(c)}\exp\left[-\frac{\tau^2}{T^2(c)}\right] \\ & \times \exp\left[-\frac{\left(\omega-2\omega_0\right)^2}{\Omega^2}\right], \end{aligned} \tag{29}$$

where $G_0 = 2\pi^3\left|A_0\right|^4\Omega^2$. In view of Eq. (29), we can directly determine the pulse duration $T(c)$ from the τ axis and the spectral width Ω from the $\omega-2\omega_0$ axis of the single-shot spectrogram, when the incident pulse is a chirped Gaussian.

Let us next consider multi-shot SHG FROG measurements by inserting Eq. (29) into Eq. (26). We then have explicitly

$$\begin{aligned} G(\omega,\tau) = {} & G_0\exp\left[-\frac{\left(\omega-2\omega_0\right)^2}{\Omega^2}\right] \\ & \times \int_{-\infty}^{\infty}\frac{p(c)}{\sqrt{1+\Omega^4c^2}}\exp\left[-\frac{(\tau/T)^2}{1+\Omega^4c^2}\right]\mathrm{d}c. \end{aligned} \tag{30}$$

The multishot spectrogram is therefore similar to the single-shot spectrogram along the frequency axis. However, the distribution along the τ axis is modified, depending on the explicit form of $p(c)$. Assuming a uniform distribution, as in Eq. (13), and employing a normalized variable $c' = c\Omega_\mathrm{p}^2$ gives, at $\omega = 2\omega_0$,

$$\begin{aligned} G(2\omega_0,\tau) = {} & G_0\int_{-1/2}^{1/2}\left[1+\left(\Omega/\Omega_\mathrm{p}\right)^4c'^2\right]^{-1/2} \\ & \times \exp\left[-\frac{(\tau/T)^2}{1+\left(\Omega/\Omega_\mathrm{p}\right)^4c'^2}\right]\mathrm{d}c'. \end{aligned} \tag{31}$$

Clearly the distribution of $G(2\omega_0,\tau)$ depends uniquely on the ratio Ω/Ω_p. Therefore, if we know *a priori* that the pulse train is circularly correlated, this ratio (giving the degree of coherence) can be retrieved from the multishot spectrogram.

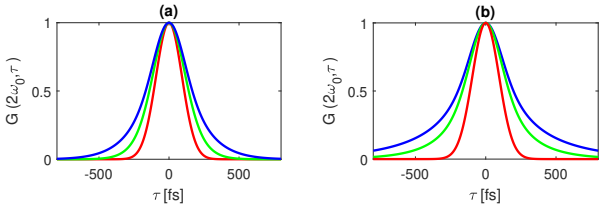

Figure 3. Time-delay cross sections at $\omega = 2\omega_0$ of multishot SHG FROG spectrograms of (a) circularly and (b) nonuniformly correlated pulse trains with different degrees of coherence. Red: $\omega_0/\Omega_\mathrm{p} = 100$, green: $\omega_0/\Omega_\mathrm{p} = 300$, and blue: $\omega_0/\Omega_\mathrm{p} = 400$.

Similar conclusions hold also for nonuniformly correlated pulse trains following Eq. (21), for which

$$\begin{aligned} G(2\omega_0,\tau) = {} & \frac{G_0}{\sqrt{\pi}}\int_{-\infty}^{\infty}\exp\left(-c'^2\right)\left[1+\left(\Omega/\Omega_\mathrm{p}\right)^4c'^2\right]^{-1/2} \\ & \times \exp\left[-\frac{(\tau/T)^2}{1+\left(\Omega/\Omega_\mathrm{p}\right)^4c'^2}\right]\mathrm{d}c'. \end{aligned} \tag{32}$$

Some cross-sections $G(2\omega_0, \tau)$ are illustrated in Fig. 3.

4. Experimental results

To verify the proposed method for generating temporally partially coherent pulse trains, we performed a set of proof-of-concept experiments. An unfolded schematic of the setup that was employed to modulate the spectral phase of pulses from a mode-locked femtosecond laser (Quantronix Integra C-5 with center wavelength 792 nm) is presented in Fig. 4. The incident pulses were first passed through a linear polarizer, after which the light was dispersed to a spectrum with a grating (Thorlabs GR25-1208) with 1200 lines/mm and a cylindrical Fourier transform lens (f = 100 mm). The spectrum was then modulated with a phase-only reflective SLM (Hamamatsu X13267-02 LCOS, 800 × 600 pixels with pitch 12.5 μm). The reflected light followed the same path as the incident pulse train, but was slightly shifted in the direction perpendicular to the plane. This allows the modulated light to be picked by mirror M_2, which fed the pulses into a commercial SHG FROG device (GRENOUILLE 8-50 USB).

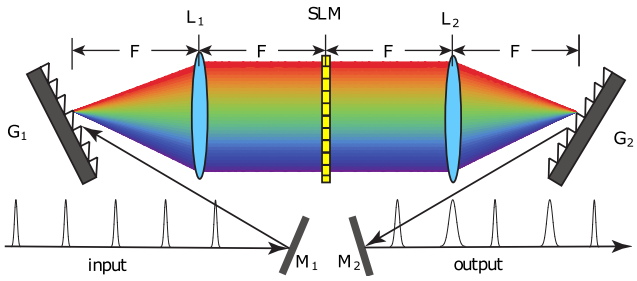

Figure 4. Schematic of the unfolded experimental setup. G_1, G_2: gratings, L_1, L_2: lenses, M_1, M_2: mirrors, SLM: a reflective phase-only spatial light modulator.

Although the employed setup is essentially a zero-dispersion pulse compressor, the input pulses did experience some broadening as they propagated through the setup. The broadening was due to alignment errors [38]. In addition, the input pulses were not perfectly transform-limited (i.e., shortest possible for the given spectrum). To counteract this, we measured the unmodulated pulses to find their spectral phase. Addition of an opposite 'base phase' in the SLM allowed us to achieve nearly flat phase across the spectrum, yielding nearly transform-limited pulses, as shown in Fig. 5, where the blue line depicts the field, and the red line corresponds to the phase. The full width half maximum (FWHM) width of the uncompressed pulses was 150 fs (see Figs. 5(a) and (b)), whereas after compression the pulse width was 130 fs (see Figs. 5(c) and (d)), which is the manufacturer-specified minimum pulse length.

The measured spectral phase corresponded well with the desired phase and there were no significant distortions. The spatial profile of the beam was roughly Gaussian, and it remained the same shape at the output as it was at the input. Moreover, the spot size on the SLM in our experiments was small enough so that the spatial distribution at each wavelength experienced an almost constant phase. Thus, the spatial coherence and the spatial intensity distribution at the output were essentially unmodified.

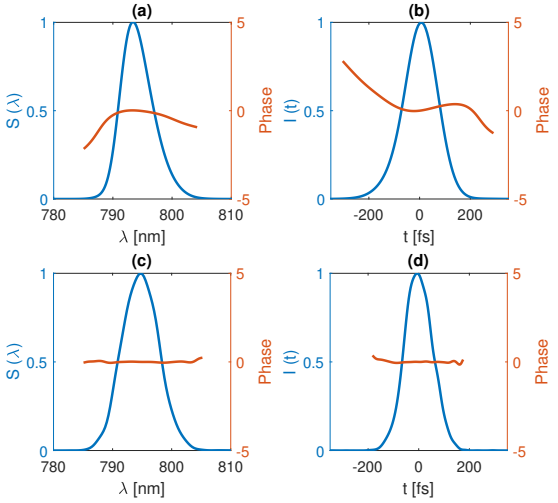

Figure 5. The measured pulse-profiles before compression in (a) spectral and (b) temporal domains, and after compression likewise in (c) and (d). The blue lines show the absolute values of the spectral and temporal fields, and the corresponding phases are shown in red.

To check the stability of the transform-limited pulse train, we measured 50 individual pulses by intensity triggering the GRENOUILLE via software. The repetition rate of the laser was 1 kHz, and thus, by keeping the exposure time less than 1 ms it was possible to obtain FROG traces of single pulses. After computing the correlation functions, we found that the incident pulses are indeed almost similar, and the normalized correlation functions have values close to unity in the region where the (spectral or temporal) intensity is significant. Thus, we conclude that the pulse train incident on our experimental setup is almost completely temporally and spectrally coherent, as far as our measurement setup can detect. Note that we have not considered the carrier-envelope offset phase or timing jitter in our theoretical calculation, since the GRENOUILLE cannot detect either.

Starting from the compressed pulses, we produced partially coherent pulse trains via time dependent spectral phase control. Since the compressed pulses in Fig. 5 are not exactly of transform-limited Gaussian form, slight deviations between the experiments and theory were to be expected. We changed the curvature

c of the quadratic phase profile and performed single-shot measurements with GRENOUILLE, such that each measured pulse has a different spectral phase. For all retrievals, the FROG error was between 1-3 percent which is well within acceptable limits. The value of c was changed following either uniform or Gaussian distribution within the range from 0 to $\sim 100 \times 10^{-28}$ s^2.

It needs to be noted that the frame rate of the SLM was too slow to follow the 1 kHz repetition rate of the laser. Therefore we were not able to modulate each pulse separately. Instead, we measured longer segments of the train having identical pulses. While every segment is completely coherent, the whole pulse train with N segments is partially coherent. This is mathematically equivalent to reducing the repetition rate by using an electro-optic modulator and observing direct multi-shot spectrograms.

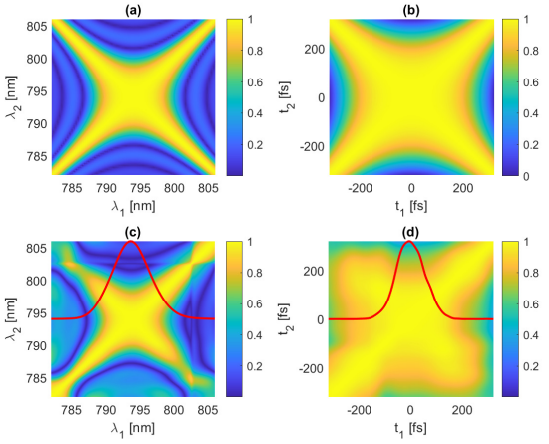

Figure 6. Simulated and experimental complex degrees of coherence of circularly correlated pulse train showing (a) and (b) the simulated results in spectral and temporal domain, respectively, whereas (c) and (d) are the corresponding experimental results. Red curves denote the intensity profiles in the spectral and temporal domain.

The complex degrees of coherence were computed from the measured ensembles and compared with the simulated ones as presented in Fig. 6 for circularly correlated pulse trains and in Fig. 7 for nonuniformly correlated pulse trains with $\Omega_p = \omega_0/150$. The simulated and experimentally observed absolute values of the complex degrees of coherence in both spectral and temporal domains are in good agreement. There is a slight asymmetry in the measured spectral domain correlations, which is due to the non-Gaussian and asymmetric spectral shape of the incident pulses.

Finally, in Fig. 8 we present the effect of time-dependent spectral phase modulation on the SHG FROG spectrograms of circularly correlated pulses for both single-shot and multi-shot simulations and measurements. First of all, from the single-shot

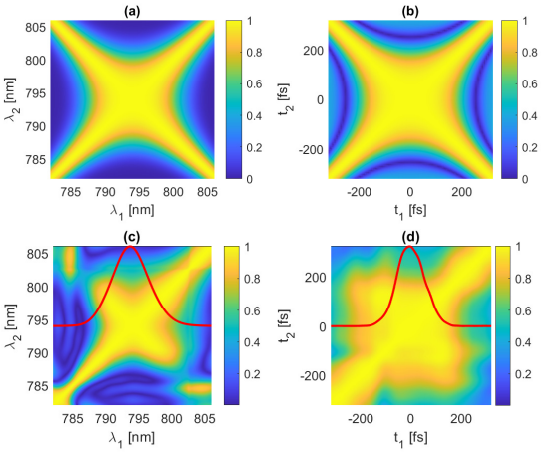

Figure 7. Simulated and experimental complex degrees of coherence of nonuniformly correlated pulse train showing (a) and (b) the simulated results in spectral and temporal domain, respectively, whereas (c) and (d) are the corresponding experimental results. Red curves denote the intensity profiles in the spectral and temporal domain.

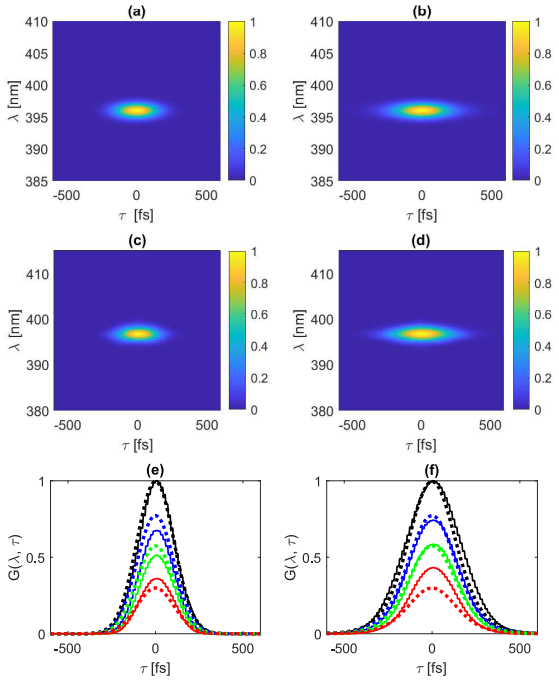

Figure 8. Simulated and measured single-shot (for the transform-limited pulse) (a, c, e) and multi-shot (b, d, f) results. (a) and (b) present the full 2D plots of simulated spectrograms, (c) and (d) illustrate the corresponding measured spectrograms. (e) and (f) show some line profiles in the central region of the FROG spectrogram, black: 396 nm, blue: 395.5 nm, green: 395 nm, and red: 394.5 nm, where solid line represents simulated results and dotted line shows experimental results.

measurement (see Fig. 8(c)), the temporal and spectral pulse widths of the transform-limited pulse, T and Ω, can be found. This step is not necessary for finding the correlation properties of the pulse train, since the

coherence functions do not depend on either T or Ω, see Eqs. (15) and (23). From the multi-shot SHG FROG spectrogram (Fig. 8(d)) we find $G(\tau, 2\omega_0)$, the black dotted line in Fig. 8(f), which we use to find Ω_p by fitting Eq. (31) on the measured curve.

The experimental values retrieved from the measured spectrograms are $\Omega = 1.33 \times 10^{13}$ s^{-1} and $\Omega_\mathrm{p} = 6.93 \times 10^{12}$ s^{-1}. The root-mean-square (rms) error between the measured and simulated multi-shot spectrograms is about 1.8 %, and there is clearly a good agreement between the theoretical and experimental results, although the spectra of the two are not exactly the same. The main difference can be seen in the amplitudes of the curves, whereas the widths have a good correspondence.

5. Conclusions and discussion

In the present work we have demonstrated controlled generation of temporally partially coherent pulse trains via time dependent spectral phase modulation. This marks a decisive experimental demonstration of controlled nonconventional temporal coherence of pulse trains and its confirmation by means of direct FROG spectrograms. The type of correlation in our scheme can be changed by suitably choosing the modulating phase profile, whereas the degree of coherence depends only on the chosen weight function. The main limitation of our method is the modulation speed, since SLMs are generally not fast enough (highest frame rate is 120 Hz or so, which is not nearly enough for modulating single pulses even in our setup). In this regard, one option to increase it considerably is to use acousto-optic modulators [38], in analogy with coherence modulation in the spatial domain [46]. This would require a somewhat different analysis approach (not considered here). However, when the observation time is much longer than the modulation switching time, the train is effectively partially coherent. This is analogous to controlling the spatial coherence with a rotating diffuser: if the diffuser does not rotate fast enough, then one can observe the coherent speckle patterns at the observation plane. When integrating over a long measurement time, we emulate partial spatial coherence.

The ability to generate nonconventional temporal correlations such as circularly and nonuniformly correlated pulse trains will facilitate in-laboratory observation of the theoretically predicted properties of such pulse trains, including temporal self-focusing. Although we concentrate here on quadratic phase modulation, any type of spectral phase profiles may be employed. The technique can therefore be readily extended to the generation of other partially coherent pulse trains that have been studied theoretically. Expanding this technique to vectorial partially coherent trains would allow further control over the correlation properties of the pulse train, which is a research direction we aim to explore in the near future.

Acknowledgements

This work is part of the Academy of Finland Flagship Program 'Photonics Research and Innovation' (PREIN), projects (320165, 320166), and is partly funded by Academy of Finland projects (308393, 310511, 321066, and 333938), National Natural Science Foundation of China (12174171), as well as the Central Plains Talents Program of Henan (ZYYCYU202012144), and the High-Level Talents International Training Program of Henan.

Disclosures

The authors declare no conflict of interest.

Data Availability

Data underlying the results presented in this paper are not publicly available at this time but may be obtained from the authors upon reasonable request.

Acknowledgements

Academy of Finland (projects 285880, 308393, and 310511). This work is part of the Academy of Finland Flagship Program, Photonics Research and Innovation (PREIN, project 320166).

References

[1] Mandel L and Wolf E 1995 *Optical Coherence and Quantum Optics* (Cambridge University Press)
[2] Gbur G and Visser T D 2010 The structure of partially coherent fields in *Progress in Optics* vol. 55 E. Wolf ed. (Elsevier) pp. 285–341
[3] Lajunen H and Saastamoinen T 2011 Propagation characteristics of partially coherent beams with spatially varying correlations *Opt. Lett.* **36** 4104–4106
[4] Mei Z 2014 "Light sources generating self-focusing beams of variable focal length *Opt. Lett.* **39** 347–350
[5] Song Z, Liu Z, Zhou K, Sun Q and Liu S 2015 Propagation characteristics of a non-uniformly Hermite–Gaussian correlated beam *J. Opt.* **18** 015606
[6] Mei Z and Korotkova O 2013 Cosine-Gaussian Schell-model sources *Opt. Lett.* **38** 2578–2580
[7] Chen Y, Gu J, Wang F and Cai Y 2015 Self-splitting properties of a Hermite-Gaussian correlated Schell-model beam *Phys. Rev. A* **91** 013823
[8] Chen Y, Ponomarenko S A and Cai Y 2017 Self-steering partially coherent beams *Sci. Rep.* **7** 39957

[9] Korotkova O, Sahin S and Shchepakina E 2012 Multi-Gaussian Schell-model beams *J. Opt. Soc. Am. A* **29** 2159–2164

[10] Sahin S and Korotkova O 2012 Light sources generating far fields with tunable flat profiles *Opt. Lett.* **37** 2970–2972

[11] Mei Z and Korotkova O 2013 Random sources generating ring-shaped beams *Opt. Lett.* **38** 91–93

[12] Korotkova O 2014 Random sources for rectangular far fields *Opt. Lett.* **39** 64–67

[13] Mei Z 2014 Two types of sinc Schell-model beams and their propagation characteristics *Opt. Lett.* **39** 4188–4191

[14] Wang F and Korotkova O 2016 Random sources for beams with azimuthal intensity variation *Opt. Lett.* **41** 516–519

[15] Li J, Wang F and Korotkova O Random sources for cusped beams 2016 *Opt. Express* **24** 17779–17791

[16] Mei Z and Korotkova O 2017 Random sources for rotating spectral densities *Opt. Lett.* **42** 255–258

[17] Ding C, Korotkova O, Zhang Y and Pan L 2014 Cosine-Gaussian correlated Schell-model pulsed beams *Opt. Express* **22** 931–942

[18] Pesonen H, Saastamoinen K, Koivurova M, Setälä T and Turunen J 2019 Temporal coherence modulation of pulsed, scalar light with a Fabry-Pérot interferometer *J. Opt. Soc. Am. A* **36** 1137–1145

[19] Pesonen H, Li P, Setälä T and Turunen J 2020 Temporal coherence and polarization modulation of pulse trains by resonance gratings *J. Opt. Soc. Am. A* **37** 27–38

[20] Wang H, Ji X-L, Deng Y, Li X-Q and Yu H 2020 Theory of the quasi-steady-state self-focusing of partially coherent light pulses in nonlinear media *Opt. Lett.* **45** 710–713

[21] Shirai T, Setälä T and Friberg A T 2010 Temporal ghost imaging with classical non-stationary pulsed light *J. Opt. Soc. Am. B* **27** 2549–2555

[22] Abbas A, Xu C and Wang L-G 2020 Spatiotemporal ghost imaging and interference *Phys. Rev. A* **101** 043805

[23] Hannonen A, Shevchenko A, Friberg A T and Setälä T 2020 Temporal phase-contrast ghost imaging *Phys. Rev. A* **102** 063524

[24] Gao Y, Cui Y, Ji L, Rao D, Zhao X, Li F, Liu D, Feng W, Xia L, Liu J, Shi H, Du P, Liu J, Li X, Wang T, Zhang T, Shan C, Hua Y, Ma W, Sun X, Chen X, Huang X, Zhu J, Pei W, Sui Z and Fu S 2020 Development of low-coherence high-power laser drivers for inertial confinement fusion *Matter Radiat. Extremes* **5** 065201

[25] Gao Y, Ji L, Zhao X, Cui Y, Rao D, Feng W, Xia L, Liu D, Wang T, Shi H, Li F, Liu J, Du P, Li X, Liu J, Zhang T, Shan C, Hua Y, Ma W, Sui Z, Zhu J, Pei W, Fu S, Sun X and Chen X 2020 High-power, low-coherence laser driver facility *Opt. Lett.* **45** 6839–6842

[26] Zhong Z, Li B, Xiong H, Li J, Qiu J, Hao L and Zhang B 2021 Effective optical smoothing scheme to suppress laser plasma instabilities by time-dependent polarization rotation via pulse chirping *Opt. Express* **29** 1304–1319

[27] Ding C, Koivurova M, Turunen J and Pan L 2018 Temporal self-splitting of optical pulses *Phys. Rev. A* **97** 053838

[28] Ma R, Li J Q, Guo J Y, Wu H, Zhang H H, Hu B, Rao Y J and Zhang W L 2019 High-power low spatial coherence random fiber laser *Opt. Express* **27** 8738–8744

[29] Huang Y, Chen H, Fontaine N K, Zhang Y, Huang H, Mazur M, Alvarado-Zacarias J C, Ryf R, Neilson D T, Li G, Amezcua-Correa R, Carpenter J, Song Y and Wang M 2021 Optical broadcasting employing incoherent and low-coherence spatial modes for bi-directional optical wireless communications *J. Light. Technol.* **39** 833–838

[30] Tang M, Zhao D, Zhu Y and Ang L-K 2016 Electromagnetic sinc Schell-model pulses in dispersive media *Phys. Lett. A* **380** 794–797

[31] Ding C, Korotkova O, Zhao D, Li D, Zhao Z and Pan L 2020 Propagation of temporal coherence gratings in dispersive medium with a chirper *Opt. Express* **28** 7463–7474

[32] Bertolotti M, Ferrari A and Sereda L 1995 Coherence properties of nonstationary polychromatic light sources *J. Opt. Soc. Am. B* **12** 341–347

[33] Sereda L, Bertolotti M and Ferrari A 1998 Coherence properties of nonstationary light wave fields *J. Opt. Soc. Am. A* **15** 695–705

[34] Dutta R, Turunen J and Friberg A T 2015 Michelson's interferometer and the temporal coherence of pulse trains *Opt. Lett.* **40** 166–169

[35] Ding C, Koivurova M, Turunen J, Setälä T and Friberg A T 2017 Coherence control of pulse trains by spectral phase modulation *J. Opt.* **19** 095501

[36] Trebino R *Frequency-Resolved Optical Gating: The Measurement of Ultrashort Laser Pulses* (Kluwer Academic Publishers)

[37] Bourassin-Bouchet C and Couprie M E 2015 Partially coherent ultrafast spectrography *Nat. Commun.* **6** 6465

[38] Weiner A M 2000 Femtosecond pulse shaping using spatial light modulators *Rev. Sci. Instruments* **71** 1929–1960

[39] Santarsiero M, Martínez-Herrero R, Maluenda D, de Sande J C G, Piquero G and Gori F 2017 Partially coherent sources with circular coherence *Opt. Lett.* **42** 1512–1515

[40] Santarsiero M, Martínez-Herrero R, Maluenda D, de Sande J C G, Piquero G and Gori F 2017 Synthesis of circularly coherent sources *Opt. Lett.* **42** 4115–4118

[41] Cai Y, Chen Y and Wang F 2014 Generation and propagation of partially coherent beams with nonconventional correlation functions: a review [Invited] *J. Opt. Soc. Am. A* **31** 2083–2096

[42] Lajunen H and Saastamoinen T 2013 Non-uniformly correlated partially coherent pulses *Opt. Express* **21** 190–195

[43] Gori F and Santarsiero M 2007 Devising genuine spatial correlation functions *Opt. Lett.* **32** 3531–3533

[44] Gori F, Guattari G, Palma C and Padovani C 1988 Specular cross-spectral density functions *Opt. Commun.* **68** 239–243

[45] Partanen H, Sharmin N, Tervo J and Turunen J 2015 Specular and antispecular light beams *Opt. Express* **23** 28718–28727

[46] J. Turunen, E. Tervonen, and A. T. Friberg, Acousto-optic control and modulation of optical coherence by synthetic holographic gratings, *J. Appl. Phys.* **67**, 49-59 (1990)